



Aligned α -FeOOH nanorods anchored on a graphene oxide-carbon nanotubes aerogel can serve as an effective Fenton-like oxidation catalyst



Yuyang Liu^a, Xuemin Liu^a, Yaping Zhao^{a,*}, Dionysios D. Dionysiou^{b,*}

^a School of Ecological and Environmental Science, Shanghai Key Laboratory for Urban Ecological Processes and Eco-Restoration, East China Normal University, Shanghai 200241, China

^b Environmental Engineering and Science Program, Department of Biomedical, Chemical and Environmental Engineering (DBCEE), 705 Engineering Research Center, University of Cincinnati, Cincinnati, OH, USA

ARTICLE INFO

Article history:

Received 5 January 2017

Received in revised form 21 April 2017

Accepted 4 May 2017

Available online 4 May 2017

Keywords:

Carbon-based aerogel

Goethite nanorods

photo-Fenton reaction

Refractory organics

Self-assembly

Textile wastewater

ABSTRACT

The self-assembled synthesis of a hierarchical graphene oxide (GO)-carbon nanotubes (CNTs)- α -FeOOH decorated composite aerogel (α -FeOOH@GCA) through a facile in-situ hydrolysis route is reported for the first time and the materials was tested for its performance as Fenton-like catalyst. The introduction of GO-CNTs clearly mediated the morphology to aligned α -FeOOH nanorods (*ca.* 100 nm) within aerogel matrix comparing with pristine urchin-like α -FeOOH three-dimensional microstructures (*ca.* 1 μ m). This three dimensional porous aerogel network provided efficient charge/mass-transfer leading to great enhancement of the catalytic activity of α -FeOOH. The outstanding catalytic performance of this composite in degradation of organics with different charge and structure, i.e. Orange II (OII), rhodamine B (RhB), methylene blue (MB), phenol and endocrine disruptor bisphenol A (BPA) was demonstrated. For example, the discoloration of OII with pseudo first-order rate constant of 0.10 min⁻¹ significantly exceeded that of pristine α -FeOOH. At relatively low concentration of α -FeOOH@GCA catalyst (125 mg L⁻¹) and H₂O₂ (0.55 mM) showed excellent catalytic activity for efficient (\sim 99%) discoloration of OII (40 mg L⁻¹) under a 60 min UV₃₆₅ irradiation in the pH range 3–10. The different charge of five target contaminants greatly determined the surface-catalyzed degradation kinetics at natural solution pH in the order of cationic > neutral > anionic organics due to the negatively charged carbon-based aerogel matrix. The new identified desulfonation intermediates elucidated through UPLC–MS analysis indicated two reaction pathways: 1) hydroxylation and 2) desulfonation by-products followed by cleavage of the azo bond as the predominant degradation pathway of OII. The elimination of the acute toxicity of the parent contaminant to luminescent bacterium Q67 was consistent with the formation of less toxic degradation by-products identified. Free radical quenching studies accessed the role of hydroxyl radical (\cdot OH), superoxide anion radical (O₂^{•-}) and singlet oxygen (¹O₂) as the dominating reactive oxygen species (ROS). The quantitative studies to measure radical concentrations using relative molecular probes showed the effective activation of H₂O₂ led to high rate production of ROS accounted for OII degradation. The greatly enhanced photocatalytic property of this hybrid was correlated with the efficient conversion between Fe²⁺/Fe³⁺ and synergistic coupling between α -FeOOH and carbon-based aerogel matrix evidenced through the formation of Fe–O–C chemical bonds was verified by X-ray photoelectron (XPS) analysis. Based on its simple and scalable preparation route as well as its excellent UV₃₆₅ or visible light-responsive catalytic performance, this hybrid exhibits a high potential to be used as an efficient and environmental-friendly catalyst for water remediation.

© 2017 Elsevier B.V. All rights reserved.

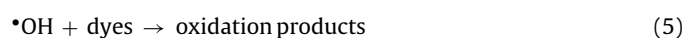
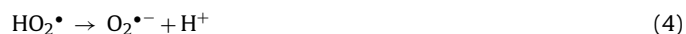
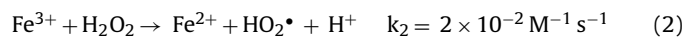
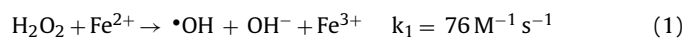
1. Introduction

Increasing discharges of refractory and toxic organic pollutants potentially threaten human health and the environment. Advanced oxidation processes (AOPs) have been regarded as efficient methods to destroy water organic pollutants using highly reactive free

* Corresponding authors.

E-mail addresses: ypzhao@des.ecnu.edu.cn (Y. Zhao), dionysios.d.dionysiou@uc.edu (D.D. Dionysiou).

radicals. Since 1964 there has been successful demonstration of oxidation of phenol in wastewater using hydroxyl radicals formed through the activation of H_2O_2 by Fe^{2+} in a homogeneous Fenton reaction. This process has gained wide attention due to its general applicability. Compared with conventional treatment processes, the photo-Fenton process is considered highly efficient, environmentally benign, and relatively inexpensive. The process achieves degradation of recalcitrant organics through oxidation by in-situ generation of hydroxyl radicals ($\bullet\text{OH}$) and/or superoxide radicals ($\text{HO}_2\bullet/\text{O}_2\bullet^-$) as described in the following reactions:



As the Fe^{2+} is rapidly depleted, these processes form large amounts of iron-containing sludge, and the catalytic activity gradually terminates. The generation of Fe^{2+} or efficient cycling of $\text{Fe}^{3+}/\text{Fe}^{2+}$ shown in Eq. (2) is the rate-determining step in the Fenton process. The efficiency of generation $\bullet\text{OH}$ in Fenton oxidation process strongly depends on maintaining an acidic pH. The research focus in advanced oxidation processes therefore involves seeking efficient and durable catalysts active over a wide pH range which are visible light responsive [1].

One of the best-known heterogeneous Fenton catalyst is iron (hydr)oxides nanoparticles. Among them, goethite ($\alpha\text{-FeOOH}$) catalyzed environmental remediation applications have been of high interest in recent years. Goethite ($\alpha\text{-FeOOH}$) is a preferred catalyst due to its nontoxicity, abundance, low cost, narrow band gap, high stability, and peroxidase-like activity [2–4]. Heterogeneous photo-Fenton catalysis mostly takes place on the surface of the catalyst, so the performance of catalysts is hampered by aggregation of the small particles, poor dispersibility, difficult separation from water, and rapid recombination of photo-induced carriers. The degradation rate of organic compounds primarily depends on the properties of the catalyst such as its crystallinity, morphology, surface area, and the properties of the catalyst's support matrix. Those support matrices greatly influence the physicochemical properties and electronic structure of the catalyst itself and play a key role in enhancing adsorption and diffusion of substrates toward accessible sites [5–9]. Resin, Nafion membrane, clay, bentonite, zeolite, and activated carbon are common support matrix materials currently studied. It is essential to find an ideal support to immobilize iron (hydr)oxides so as to improve or even enhance their catalytic performance. The synthesis of advanced composite materials is one of the most effective approaches to improve the catalytic efficiency of pristine $\alpha\text{-FeOOH}$ nanoparticles.

Graphene aerogel is a new category of carriers offering a porous 3D framework, large surface-to-volume ratio, superior electron mobility, excellent conductivity, mechanical stability, and good adsorption [10]. Its two-dimensional layered structure with sp^2 - and sp^3 -hybridized carbon atoms arranged in hexagonal rings [11,12] makes graphene a useful building block for controllable self-assembly of matrices with various architectures. Graphene aerogels effectively prevent stacking of the graphene sheets. To tailor the nanostructure, porosity, and functionality of graphene aerogel, the graphene aerogel framework can be modified by introducing metal oxide nanoparticles [13,14], carbon nanotubes or other carbon-based materials [15,16], or conductive polymer such as polypyrrole (Ppy) or polyvinyl alcohol (PVA) [17]. Metal oxide nanoparticles enhance the catalytic activity of common two-dimensional (2D) hybrid graphene composites due to 1) π - π stacking and electrostatic interaction between graphene and the organic substrates; 2)

efficient separation of photogenerated carriers and enhanced transfer of photo-induced carriers; and 3) the nanoscale miniaturization of catalytic metal growth centers, resulting in a relatively high specific surface area and relatively high redox potential. Common 2D graphene-metal oxide composites are subject to close stacking of graphene sheets and to form irreversible agglomerates during their preparation and drying. This limits the accessible surface area which leads to a great loss of active sites. This is why fabrication of 2D graphene layered building blocks into 3D macroscopic functional aerogels is a better approach.

Currently, self-assembly of 3D graphene-based aerogels involves hydrothermal methods which rely on strong π - π interaction [18], organic linkers through sol-gel polymerization [19] or reduction of graphene oxide (GO) employing chemical methods [20]. Recently, Fe_3O_4 deposited 3D graphene aerogels have been obtained through reduction by NaHSO_3 and self-assembly of a mixture of graphene oxide and colloidal Fe_3O_4 . The stability of this hybrid composite is questionable due to the weak interaction between graphene and Fe_3O_4 [21]. Moreover, the metallic Fe_3O_4 may decrease electrical conduction between the graphene layers.

A group led by Ye has fabricated graphene/pyrrole aerogels (GPAs) via a complicated two-step method in which pyrrole monomer is captured by graphene sheets during the hydrothermal self-assembly process, followed by polymerization of the adsorbed monomer [17]. It is hard to design and control the structure of the pyrrole polymer, which significantly impacts the properties of the resulting GPAs. More recently, Cong's group has reported integrating GO nanosheets into 3D macroscopic graphene aerogel devices through self-assembly induced by metal ions during the reduction of dispersed graphene oxide [22,23]. That method would work best with CNTs inserted among the graphene layers. Such a novel hybrid aerogel should effectively prevent restacking of the graphene layers via van der Waals interactions during the reduction and yield a porous network structure with physicochemical properties different from those of the individual components. This method enables synthesis of materials with large surface area, fast mass and electron transfer kinetics, short diffusion pathways in the substrate, and good mechanical strength [15]. Beyond binary metal oxide-graphene nanocomposites, ternary materials have been developed to improve the photocatalytic efficiency and visible light absorption. Kim has reported that TiO_2 loaded on graphene/carbon nanofibers by electrospinning method show good pseudo-first order kinetics and excellent stability towards degradation of methylene blue (MB) irradiated with visible light [24]. To date, however, there has been no published report of the one-step self-assembly of ternary $\alpha\text{-FeOOH}$ decorated on GO-CNTs aerogel matrix by a facile method. Its unique structure and properties should expect the fast mass transfer and good accessibility of reactants and by-products to catalyst active sites and thus guarantee the outstanding photocatalytic performance.

GO-CNTs based composite aerogels were selected to be used as a novel support to enhance the photocatalytic performances of $\alpha\text{-FeOOH}$ catalysts in environmental application. Herein, $\alpha\text{-FeOOH}@GCA$ was facilely fabricated through Fe^{2+} -induced reduction and self-assembly of GO pillared with CNTs and decorated with $\alpha\text{-FeOOH}$ simultaneously within that structure. OII, a typical anionic dyestuff, was used as target contaminant to evaluate the photocatalytic efficiency of synthesized catalyst. The excellent morphology, structure, and physicochemical properties of $\alpha\text{-FeOOH}@GCA$ facilitated remarkable enhancement of photo-Fenton oxidation of Orange II dye much better than pristine $\alpha\text{-FeOOH}$ or Evonik Degussa P25 under UV_{365} irradiation or visible light irradiation. The photocatalytic discoloration of OII was systematically elucidated and various aspects were investigated including degradation kinetics, feasibility for application in a wide pH range, removal of organics with different structure and charge,

characterization of reactive oxygen species (ROS) generated in the process, major transformation intermediates, degradation pathway of OII, and photocatalytic mechanism of the catalyst.

2. Experimental

2.1. Reagents

Azo dye Orange II (OII), rhodamine B (RhB), methylene blue (MB), bisphenol A (BPA), phenol, ferrous sulphate ($\text{FeSO}_4 \cdot 7\text{H}_2\text{O}$), H_2O_2 (30%, v/v), methanol (MeOH) and ascorbic acid (AA) were all purchased from Sinopharm Chemical Reagent Ltd. (Shanghai). Coumarin was purchased from Aladdin Ltd. (Shanghai). Tetranitromethane (TNM) was purchased from Sigma-Aldrich (China Division, Shanghai). Natural graphite was purchased from Guangfu Chemicals (Tianjin, China) and carboxylated multi-wall carbon nanotubes (CNTs) were bought from the Chengdu Organic Chemistry Institute (Chengdu, China). All the other chemicals were of analytical grade and used as received.

2.2. Preparation and characterization of $\alpha\text{-FeOOH@GCA}$

The GO was prepared from natural powder graphite through a modified version of Hummer method [25]. The $\alpha\text{-FeOOH@GCA}$ was prepared by adding 0.400 g GO and 0.172 g CNTs into 400 mL of deionized (DI) water followed by ultrasonication for about 30 min to obtain a uniform GO-CNT dispersion. Then 7.228 g $\text{FeSO}_4 \cdot 7\text{H}_2\text{O}$ was added to the above mixture and sonicated for another 30 min. The mixture obtained was hydrolyzed in a water-bath at 95°C for 6 h to form $\alpha\text{-FeOOH@GCA}$ hydrogel. The hydrogel was washed with DI water and lyophilized in a freeze dryer (XY-FD-1, Xinyu Equipment Ltd, Shanghai) to obtain the aerogel. It was manually powdered for further use. The process is shown in Scheme 1. Pristine $\alpha\text{-FeOOH}$ was synthesized directly by hydrolysis in the absence of GO-CNTs.

The crystal structure of the $\alpha\text{-FeOOH@GCA}$ was characterized using an Ultima IV X-ray diffractometer (XRD, D/Max-2500, Rigaku, Japan) employing a $\text{Cu K}\alpha$ source at $\lambda = 1.5406 \text{ \AA}$ with scan speed of $10^\circ \text{ min}^{-1}$ between 5 and 70 angular degrees. The surface morphology was observed with a transmission electron microscope (TEM, HT7700, Hitachi, Japan) and field emission scanning electron microscope (SEM, S-4800, Hitachi, Japan). The surface area and pore size distribution were measured by nitrogen adsorption with an ASAP 2020 specific surface area analyzer (Micromeritics Instrument Corp., USA) using the Brunauer–Emmett–Teller (BET) method. Pore size was calculated using the Barrett–Joyner–Halenda (BJH) technique. UV–visible diffuse reflectance spectra were acquired using a spectrophotometer (UV–vis DRS, U-4100, Hitachi, Japan) with BaSO_4 as the reference. The pH_{zpc} of $\alpha\text{-FeOOH@GCA}$ was measured in 0.01 M KNO_3 solutions in triplicate with a Malvern Zetasizer (Malvern instruments limited, USA) as a function of pH. The functional groups of catalyst were identified through Fourier transform infrared spectroscopy (FTIR, Nicolet 8700 system, PerkinElmer Inc., USA) with the KBr pellet. The surface elements were analyzed using X-ray photoelectron spectroscopy (XPS) acquired with an Axis Ultra spectrometer (Kratos, Japan).

2.3. Photo-Fenton catalytic tests

The various advanced oxidation experiments were carried out in a cylindrical borosilicate reactor with 15 cm in diameter and 7 cm height. One 125 W high-pressure mercury lamp with a main wavelength of 365 nm (Phillips GGY125Z ballast) was set perpendicularly over the center of the reactor with radiation flux of 1.94 mW cm^{-2} . The distance between the surface of solution and the UV lamp was 15 cm. The experiments were performed by

adding 50 mg of $\alpha\text{-FeOOH@GCA}$ and H_2O_2 (0.55 mM) into 400 mL of OII solution (40 mg L^{-1} or 0.11 mM) at natural pH of reaction solutions and stirred magnetically at 20°C . When studying the effect of the initial pH on photocatalytic degradation of OII, the pH was adjusted to the desired value using 1 M HCl or 1 M NaOH. At desired time intervals, 5 mL of the reaction mixture was withdrawn and centrifuged (TG16G, Experimental Instrument Ltd., Jiangsu Province, China). The UV–vis absorbance of the sample was recorded using a UV-1102 UV–vis spectrophotometer (Tianmei Techcomp Ltd., Shanghai, China) at 484 nm, the wavelength corresponding to the maximum absorbance of OII. The overall discoloration of OII was then determined using the following equation:

$$\text{Discoloration (\%)} = (C_0 - C_t)/C_0 \times 100 \quad (6)$$

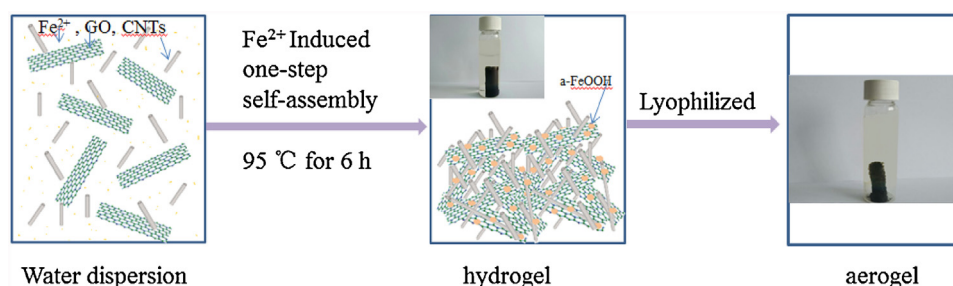
where C_0 and C_t are the concentrations of OII initially and at time t . Sulfate and nitrate anions generated during the reaction were quantified using an ion chromatography system (ICS-2500, Thermo Fisher Scientific Inc., United States). The sample's mineralization was determined by assaying the total organic carbon with a Shimadzu TOC-5050 analyzer (Shimadzu, Japan). The total dissolved iron was measured through an inductively-coupled plasma-optical emission spectroscope (ICP-OES) model OPTIMA8000 (PerkinElmer Inc., USA). The method has a detection limit of 0.030 mg L^{-1} . Decomposition of H_2O_2 was measured using the titanium (IV) oxy-sulfate method [26]. The visible light-driven catalytic degradation studies were performed by adding 100 mg of $\alpha\text{-FeOOH@GCA}$ and H_2O_2 (2.20 mM) into 400 mL of 40 mg L^{-1} solution of OII under irradiation with a 100 W iodine-tungsten lamp (Shanghai Jiguang special lighting factory, China) with radiation flux of 8.40 mW cm^{-2} .

In the experiments designed to study the role of molecule structure and charge, such as MB, RhB, OII, phenol and BPA, the initial concentrations of the organics were all 0.25 mM, and the other experimental conditions were unchanged. Acetonitrile–water co-solvent was used to improve the solubility of BPA. In the catalyst reuse experiments, six consecutive adsorption–oxidation reuse tests of the $\alpha\text{-FeOOH@GCA}$ were conducted. In each cycle, 60 min of adsorption in the dark was followed by 60 min of photo-Fenton catalytic reaction with no other post-treatment of the catalyst between tests.

Degradation intermediates of OII in $\alpha\text{-FeOOH@GCA} + \text{H}_2\text{O}_2 + \text{UV}$ system were detected by liquid chromatograph coupled with a mass spectrometer (Waters ACQUITY UPLC/MS, USA with a Waters ACQUITY UPLC BEH C18 analytical column, $1.7 \mu\text{m}$, $2.1 \times 50 \text{ mm}$). The column temperature was maintained at 25°C . There were two mobile phases: (A) 0.1% formic acid in water (v/v) and (B) acetonitrile at a flow rate of 0.6 mL/min. The gradient was as follows: 95% of phase A linearly decreasing 10% at 3.5 min, then linearly increasing to 100% and held for 0.5 min. The typical ESI–MS turbo-ion spray interface was operated in the negative or positive ion mode between m/z 100–800 with an electrospray voltage of 3 kV, a sheathing gas (N_2) flow rate of 10 L/min, a heating capillary temperature of 300°C , and a capillary voltage of 30 V.

2.4. Radical formation measurements

To elucidate the reactive oxidation species involved in this system, methanol (MeOH), ascorbic acid (AA) and sodium azide (NaN_3) were used as scavengers of hydroxyl radical ($\cdot\text{OH}$), superoxide radical ($\text{O}_2^{\cdot-}$) and singlet oxygen ($^1\text{O}_2$), respectively [27]. The quantitative generation of hydroxyl radicals was determined by coumarin through the fluorescence spectrometer at excitation wavelength of 332 nm (Hitachi F-4500, Japan) [28]. The TNM method was used to quantify the $\text{O}_2^{\cdot-}$ and the main TNM's reaction product nitroform was quantified by measuring the absorbance at 350 nm using the UV–vis spectrophotometer [29].



Scheme 1. Preparation of α -FeOOH@GCA aerogel.

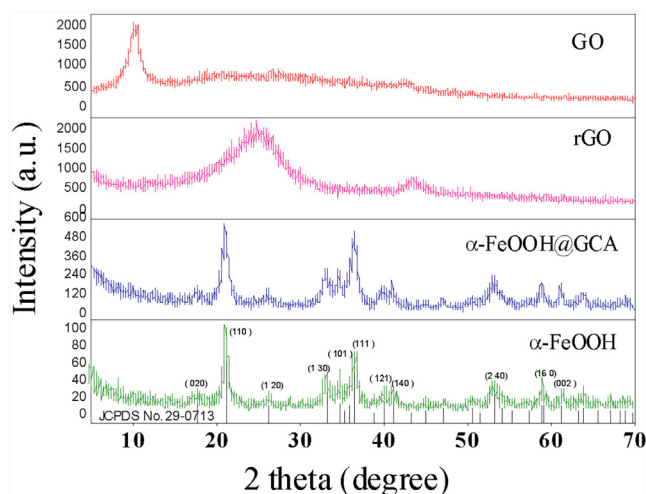


Fig. 1. X-ray diffraction spectra of GO, rGO, α -FeOOH@GCA and pristine α -FeOOH.

2.5. Toxicity measurements

Toxicity was evaluated using luminescent bacteria and a method described in previous work [30]. The luminescent bacterium Q67 (*Vibrio qinghaiensis*) cells as a freeze-dried powder were reactivated in 5 mL of 0.85% NaCl solution, and 0.05 mL of the reactivated suspension was added to 2 mL of sample. Another 2 mL containing 0.05 mL of the bacterial suspension was used as the blank. After 15 min of incubation at 20 °C, the relative luminosity of the bio-luminescent bacteria was determined using a BHP9514 drinking water safety detector at a luminescence wavelength of 490 nm.

3. Results and discussion

3.1. Characterization of the catalyst

The environmental function of goethite, one of the polymorphs of iron oxyhydroxide (FeOOH), is associated with its crystallographic phases. Fig. 1 shows the XRD diffraction patterns for the α -FeOOH@GCA, GO and regenerated graphene oxide (rGO) samples. The characteristic diffraction peak d_{001} of GO is at around $2\theta = 10.2^\circ$ and the broad peak d_{002} of rGO is at $2\theta = 26.5^\circ$. The ferrous sulfate was chosen to assist the self-assembly of α -FeOOH@GCA. The narrow and sharp diffraction peaks of pristine α -FeOOH and α -FeOOH@GCA can be assigned to a pure orthorhombic phase α -FeOOH (JCPDS No. 29-0713). The disappearing of the diffraction peaks corresponding to GO and rGO was attributed to inhibiting the restacking of graphene layers by the crystal growth of α -FeOOH and CNTs tangling around the surface of graphene oxide, which will lead to decrease the integrity of graphene oxide crystal structure. Based on the α -FeOOH@GCA diffraction peaks, the mean coherent

length of the α -FeOOH was 30.7 nm as estimated using the Scherrer equation.

The morphology and structure of the α -FeOOH@GCA were analyzed by SEM and TEM. Fig. 2a shows that the hierarchical, pristine α -FeOOH was composed of chrysanthemum-like and urchin-like hollow 3D microspheres around 1 μm . The microstructures were composed of aligned nanorods with 30–50 nm in diameter and less than 200 nm long. Fig. 2b and c shows aligned α -FeOOH microstructures embedded in-situ or decorated on the superstructure of the GO-CNT aerogel matrix in which oriented CNTs are randomly tangled with graphene sheets. The micrographs clearly show that the raft-like α -FeOOH is composed of aligned nanorods with diameters of 15–30 nm and less than 100 nm long. The small size of α -FeOOH on graphene should expose more active sites on the surface. Fe^{2+} may adsorb onto the surface of GO nanosheets due to the coordination with abundant oxygen containing groups of GO through electrostatic interactions to form Fe–O–C bonds, generating crystallization nuclei at which primary particles of α -FeOOH form. It is now generally believed that aligned α -FeOOH precipitates directly from solution in a sulfate system through the laterally-oriented crystal growth pathway with fast crystal growth kinetics. Furthermore the rafts are well aligned with several smaller nanorods which assembled through oriented, base-attached nucleation and crystal growth from small spherical primary particles [31].

The presence of dense, aligned α -FeOOH nanorods on the surface of graphene sheets is confirmed in the TEM images of Fig. 2d and f. The higher resolution inset in Fig. 2f shows the highly crystalline α -FeOOH nanorods anchored on both sides of the graphene nanosheets. The d spacing between lattice fringes of 0.245 nm were assigned to the (111) crystallographic plane of α -FeOOH. Graphene sheet does change the nucleation, growth, agglomeration, structure or size of α -FeOOH in crystal growth process, as is shown by comparison with the pristine α -FeOOH in Fig. 2a.

Apparently, GO and CNTs act as supports that can enable better distribution and stronger binding of α -FeOOH particles with the graphene sheets [32]. The CNTs and α -FeOOH uniformly disperse into the matrix to hinder aggregation of the graphene sheets and help to form abundant pores, which may be a great advantage for increasing the specific surface area and providing channels promoting mass transport [33,34]. This heterogeneous structure of α -FeOOH@GCA is not simply a physical mixture of α -FeOOH and GO-CNTs. The introduction of GO-CNTs greatly hindered the aggregation and growth of α -FeOOH crystals, forming a synergistic composite through the strong chemical interactions between α -FeOOH and the GO-CNT matrices.

The textural properties of α -FeOOH@GCA were determined through nitrogen adsorption-desorption experiments. In Fig. 3, the nitrogen adsorption-desorption isotherm of α -FeOOH@GCA shows a typical type IV curve with type 3 hysteresis loop at high relative pressure according to the IUPAC classification, which implies an irregular mesoporous structure of slit-like pores formed by aggregation of plate-like particles. The BJH pore size distribution

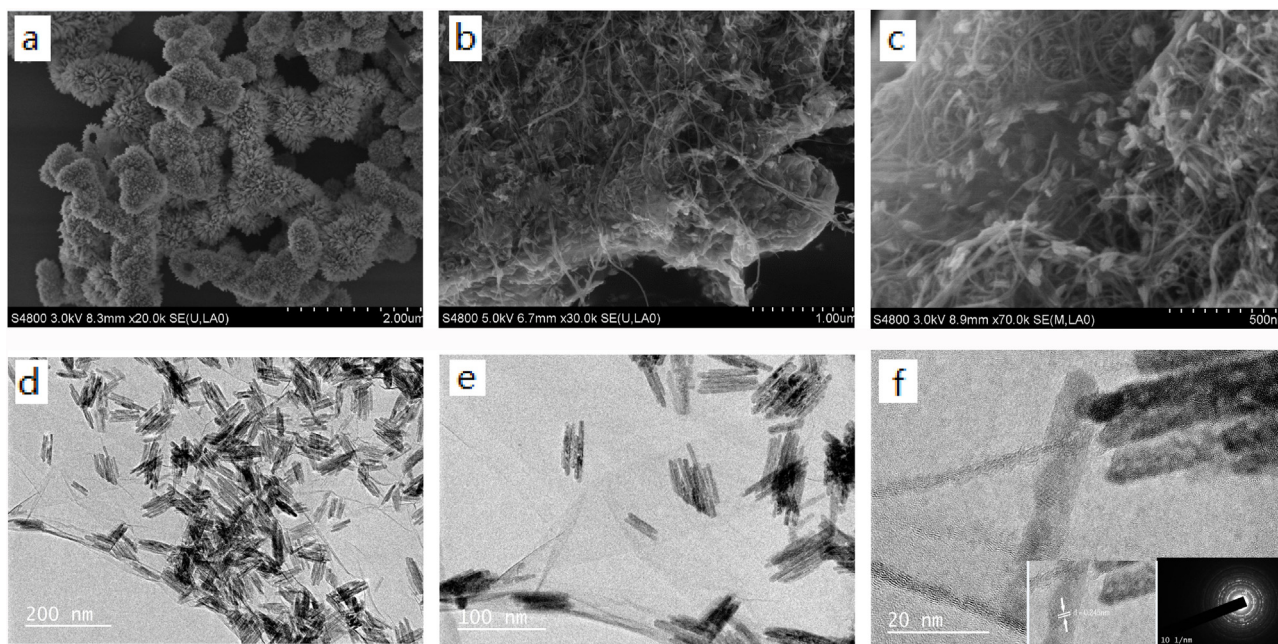


Fig. 2. SEM images of α -FeOOH (a) and α -FeOOH@GCA (b, c), TEM images of α -FeOOH@GCA (d–f) with the inset of high resolution image of the lattice fringes in (f).

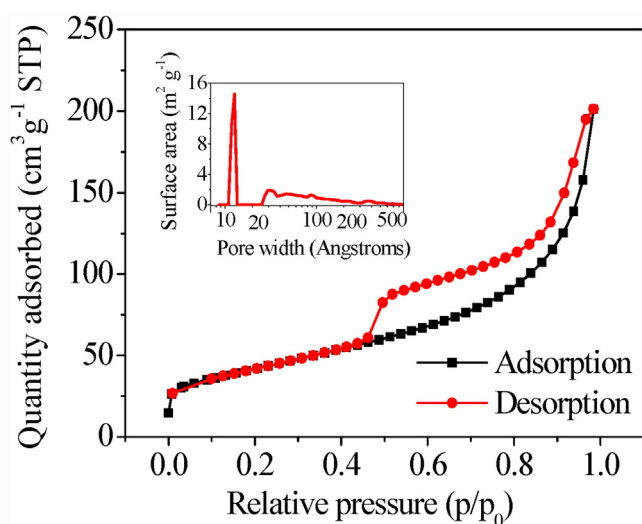


Fig. 3. Typical nitrogen adsorption-desorption isotherms for α -FeOOH@GCA with an inset of the pore size distribution curves.

(inset) shows that most of the pore volume lies within 10–80 nm, with a peak pore diameter of 1.3 nm which can be ascribed to intra-particle pores. The BET surface area of the α -FeOOH@GCA was about $150 \text{ m}^2 \text{ g}^{-1}$ with an average pore width about 8.3 nm. The relatively large surface area and abundant hierarchical pores at nanoscale was mainly assembled due to the separation of the graphene nanosheets by formed α -FeOOH and dispersed CNTs [35]. The pore volume of $0.31 \text{ m}^3 \text{ g}^{-1}$ consists of about 71% mesopores and 29% of macropores. A large surface area of course favors OII adsorption [36]. The GO-CNTs aerogel framework increases the surface area and extends the number of accessible active sites of α -FeOOH.

The optical absorption properties of pristine α -FeOOH and α -FeOOH@GCA were investigated according to their UV-vis DRS. In Fig. 4, the as-prepared pristine α -FeOOH has an absorption edge at approximately 610 nm assigned to the intrinsic narrow band gap of about 2.03 eV. α -FeOOH also has shoulder absorption about 475 nm

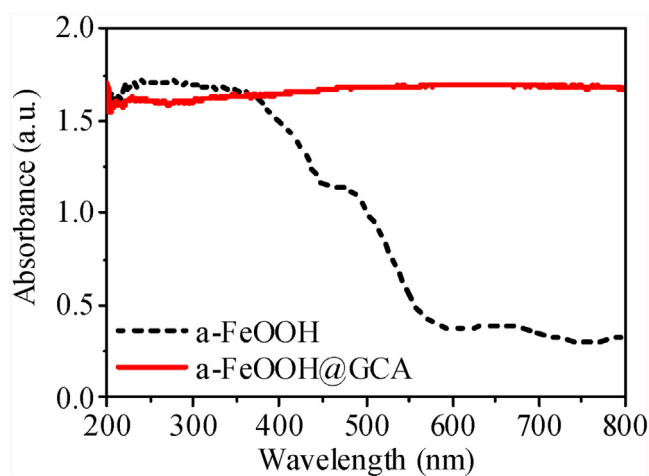


Fig. 4. UV-V DRS spectra of α -FeOOH and α -FeOOH@GCA.

which results from the photoexcited electron transition from O 2p to Fe 3d. α -FeOOH@GCA exhibits strong absorption and significant photosensitivity in UV regions and obviously enhanced light absorption efficiency in visible range, probably due to interfacial interaction between α -FeOOH and the GO-CNTs.

3.2. Photo-Fenton-like experiments

3.2.1. Discoloration of OII in α -FeOOH@GCA + H_2O_2 + UV system

A controlled experiment was carried out to evaluate the catalytic activity of the α -FeOOH@GCA. The discoloration rate of OII as a function of time under different conditions is shown in Fig. 5. The discoloration in UV photolysis was 20.1%. The discoloration in the H_2O_2 + UV system reached 90.1% due to oxidation by $\cdot\text{OH}$ generated from photolytic decomposition of H_2O_2 [37]. However, it should be noted that in spite of the relatively high discoloration, the total organic carbon removal in the H_2O_2 + UV system was negligible. The adsorption of OII on α -FeOOH and α -FeOOH@GCA was relatively fast in the dark. In the first 10 min of reaction, dis-

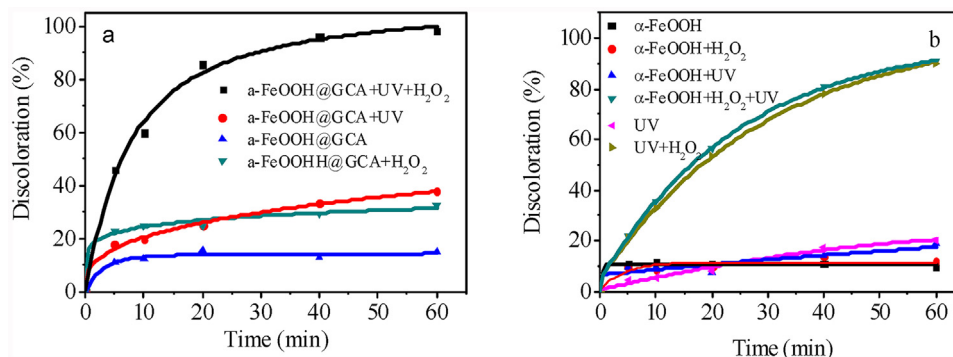


Fig. 5. Discoloration of OII with time under different experimental conditions.

coloration of 10.0% and 19.9%, respectively, was observed. The discoloration in the α -FeOOH+UV and α -FeOOH@GCA+UV photocatalytic systems was only 19.1% and 38.1%, respectively. In Fenton-like systems without UV irradiation discoloration rates of 11.7% for α -FeOOH+H₂O₂ and 32.6% for α -FeOOH@GCA+H₂O₂ were observed. The discoloration rates under UV were 60.7% and 98.3% in corresponding photo-Fenton-like systems, respectively. The quantum yield of α -FeOOH@GCA+H₂O₂+UV system used to describe the catalytic efficiency was calculated to be 3.19%. The enhanced OII discoloration was ascribed to photolysis of Fe(III)-H₂O₂ complexes on the surface [38]. Compared with pristine α -FeOOH, α -FeOOH@GCA greatly enhanced the discoloration efficiency consuming relatively small amount of H₂O₂ due to the introduction of GO-CNT aerogel matrix [39]. Comparing with the OII discoloration rate in α -FeOOH@GCA+H₂O₂+UV system, the discoloration of OII was greatly enhanced in this synergistic α -FeOOH@GCA+H₂O₂+UV system. Similarly, enhanced photocatalytic activity has been reported for graphene-based Fe₂O₃, Cu₂O, TiO₂ and ZnO [40–43]. In this study, the photo-induced electron-hole pairs of α -FeOOH recombine quickly under UV irradiation, resulting in lower photocatalytic activity. The 3D α -FeOOH@GCA framework's interconnected pores provide abundant catalytic sites and enhance substrate mass transfer. These are part of the reasons for the enhanced photocatalytic degradation rates of OII. Moreover, α -FeOOH@GCA is much easier to be separated by centrifugation because of its aerogel matrix compared to TiO₂ that usually forms a colloidal suspension. The dye discoloration process can be fitted by linear regression assuming pseudo-first-order kinetics.

$$\ln(C_t/C_0) = -k_1 \times t \quad (7)$$

where k_1 is the pseudo-first-order rate constant. Fitted kinetic models are shown in Table S1. The k_1 of the α -FeOOH@GCA+H₂O₂+UV system is nearly 2.4 times that of α -FeOOH+H₂O₂. Synergy between α -FeOOH@GCA, H₂O₂ and UV greatly improves the catalytic degradation efficiency.

3.2.2. OII mineralization

The extent of mineralization is also an important factor in practical applications. OII mineralization was quantitatively determined by total organic carbon (TOC) removal as well as by sulfate and nitrate anion formation. The results are shown in Fig. 6. The TOC removal increased rapidly, reaching 52% after 60 min. So the process gives effective mineralization of OII. SO₄²⁻ generation was detected during the initial stage of the reaction. Its concentration increased sharply during the initial 5 min and then gradually increased until 60 min, with about 74% formed in the first 5 min and 91.4% in 60 min according to stoichiometric calculations based on the sulfur contained in OII. It seems that all the sulfonic groups of the OII molecules are eventually oxidized. By contrast, the generation of NO₃⁻ was slow and nearly constant, with only about 4.7%

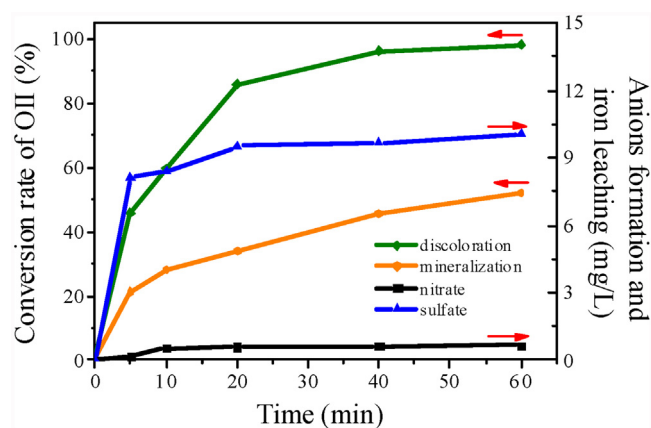


Fig. 6. Mineralization of OII with time in the α -FeOOH@GCA+H₂O₂+UV system.

conversion after 60 min as estimated from stoichiometry. The initial step in OII photocatalytic degradation seems mainly to involve the destruction of sulfonic groups on the benzene rings through hydroxyl radical attack. That is followed by the cleavage of azo bonds, damaging the conjugated π systems and leading to discoloration; the formed products undergo further degradation and are finally completely mineralized.

3.3. Initial pH

pH greatly affects the efficiency of Fenton reactions by changing the interface properties of the catalyst. The discoloration of OII as a function of initial solution pH is shown in Fig. 7. The pH_{ZPC} of α -FeOOH@GCA is about 3.4 and shown Fig. S1a. The discoloration rate decreased slightly with increasing pH due to weakening of the electrostatic attraction between OII and α -FeOOH@GCA when pH increases [44]. The hydroxylation of the catalyst's surface should not be the only determinant of the degradation kinetics. The azo group of OII will transform to a less stable quinoid structure in a solution with a pH less than 3.4, which will also contribute to faster discoloration in acidic pH range. Many previous studies have reported that the optimum solution pH is around 3, though in heterogeneous Fenton reactions α -FeOOH@GCA retains its efficiency over a wide pH range [3,6,45]. The pH during photocatalytic degradation was also measured and results are shown in Fig. S1b. When the initial pH was below ~ 9 , the pH did not change drastically during the reaction due to the strong buffer ability of the catalyst; however, when the initial pH was above ~ 11 , the pH gradually decrease to ~ 9 due to the formation of acidic reaction intermediates.

Fig. 7b shows the evolution of H₂O₂ at different pH values. The effects of pH and H₂O₂ consumption coincide, indicating that

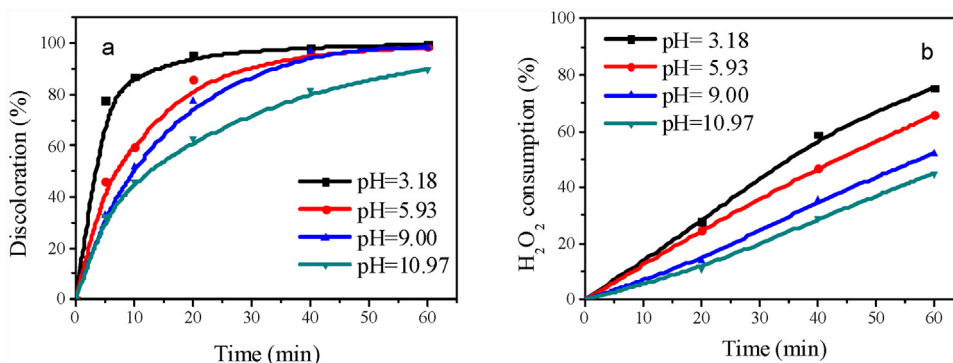


Fig. 7. Discoloration of OII (a) and H₂O₂ consumption (b) in the α -FeOOH@GCA + H₂O₂ + UV system at different initial pH values.

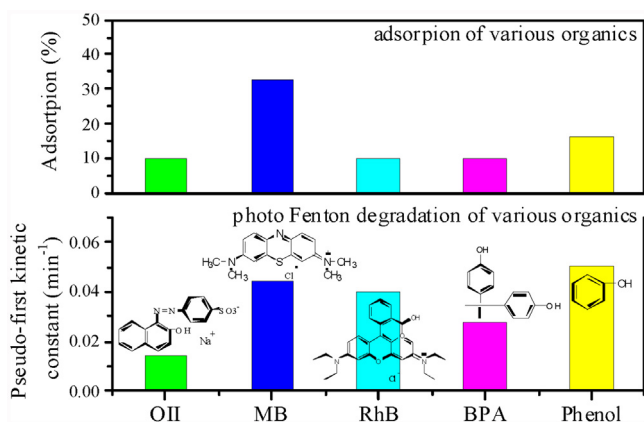


Fig. 8. Adsorption-photo-Fenton degradation of various organics in the α -FeOOH@GCA + H₂O₂ + UV system.

H₂O₂ is consumed exclusively in OII degradation and not in self-decomposition. The consumption of H₂O₂ decreased from 75.4% to 45.1% when the initial pH was increased from 3.18 to 10.97, illustrating that H₂O₂ was more likely to be activated through protonation, producing an appreciable amount of \cdot OH radicals in acidic conditions [46]. Hence, α -FeOOH@GCA can overcome this drawback of conventional homogeneous Fenton reagents and effectively expand the pH range for efficient practical applications. This has practical significance, since the costly acidification process is one of the weaknesses of Fenton reaction which limit its industrial application in treating dying wastewater.

3.4. Effectiveness in degrading various organic structures

Usually, the photocatalytic degradation rates can be described by pseudo-zero-order kinetics because the amount of H₂O₂ was excessive and the mass transfer of high concentration organics was not the rate-determining step at initial reaction time. With the depletion of the organics, the degradation rates can be described by pseudo-first-order kinetics due to the limitation of mass transfer of lower concentration organics at later reaction stage. The adsorption of organic molecules on the surface of α -FeOOH@GCA presents a significant step in the heterogeneous Fenton reaction [47], and the photo-Fenton degradation rates are a function of the amount of adsorbates. The chemical structure of the target organics has a considerable effect on the adsorption or photocatalytic degradation kinetics. It should be noted that differences in surface charge or molecular structure of organics, and catalyst's supporting matrix may play a vital role and lead to different kinetics of adsorption and photocatalytic degradation [48–50]. In Fig. 8, the oxidation rate of anionic dye OII was compared with the oxidation rates of the

cationic dyes methylene blue (MB) and rhodamine B (RhB) and the nonionic organics phenol and contaminant of emerging concern bisphenol A (BPA). The extent of adsorption (% of initial amount) was found to follow the order of MB > phenol > RhB \approx BPA \approx OII and the pseudo-first-order rate constants of photo-Fenton oxidation were found to follow the order of phenol > MB \approx RhB > BPA > OII.

As for different charged organics, α -FeOOH@GCA exhibits large adsorption capacity for cationic organic MB through electrostatic attraction and π - π interaction with the catalyst's negative charged GO-CNTs matrix, thus it exhibited higher degradation kinetics for this dye. Comparing with cationic MB with the pseudo-first order rate constant of 0.0443 min⁻¹, α -FeOOH@GCA shows relatively small degradation kinetics for nonionic or neutral BPA due to the lower adsorption capacity for BPA mainly through π - π interaction and hydrogen bond. Meanwhile, α -FeOOH@GCA shows relatively lower degradation kinetics for anionic OII due to the lower adsorption capacity for OII which was the result of electrostatic repulsion between them. It can be seen that the photo-Fenton degradation kinetics greatly depended on the type of charge of relevant organics in the order of cationic > neutral > anionic.

The degradation kinetics follow similar trend for same kind of molecule charges, such as in the case of the decomposition of the two cationic dyes: MB > RhB. Previous works also showed that anionic dyes degraded more slowly in such systems [48,51]. For MB and RhB, the more aromatic or heterocyclic rings in the molecular core structure, the higher of the steric hindrance effects of substituents [49] and the less the adsorption capacity might be. The difference in adsorption capacity of MB and RhB does not significantly influence the degradation kinetics of these two dyes. In this study, the molecule charge rather than the molecular structure has significantly influence on the degradation kinetics. Phenol is an exception, the observed fast degradation kinetics of phenol can be attributed to its simple aromatic planar hexagonal configuration with lower steric hindrance, which can allow phenol to strongly interact with the conjugated hexagonal planar GO nanosheets through π - π stacking or hydrogen bonding [52]. Comparing with phenol, the complexity of molecular structure or the adsorption capacity of BPA on this hybrid plays more important role on the lower degradation kinetics in this system. In short, the degradation kinetics of organics greatly depend on the contaminant charges in this heterogeneous photo-Fenton process due to the negatively charged supporting matrix, which greatly influences the affinity of the target contaminants to the catalyst active sites.

3.5. Durability of α -FeOOH@GCA

Adsorption-oxidation catalyst reuse experiments were carried out to test the long-term durability of the catalyst. Fig. 9 shows that the OII adsorption gradually decreased from 23.7% to 6.0%

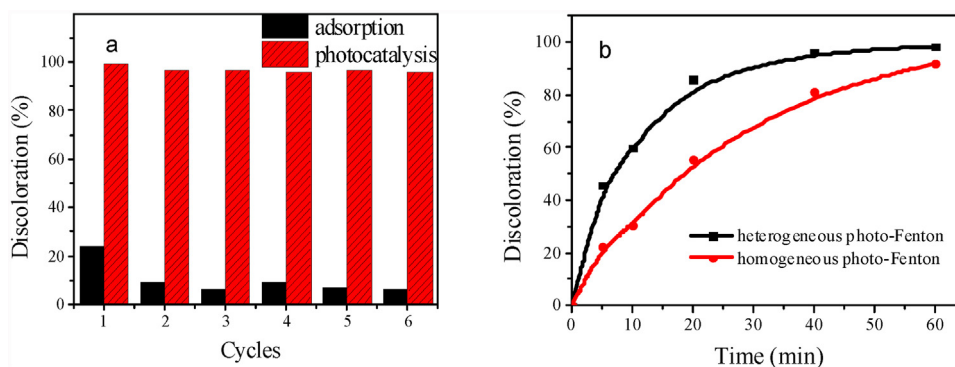


Fig. 9. Six adsorption-degradation cycles of OII (a) and the contribution of homogeneous photo-Fenton using maximum iron leaking of 0.286 mg L^{-1} (b).

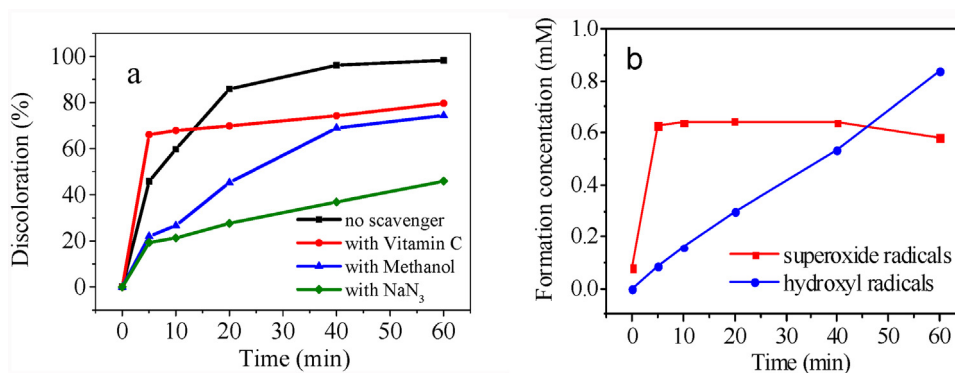


Fig. 10. Discoloration of OII in presence of radical scavengers (a) and the generation of ROS (b) in the $\alpha\text{-FeOOH@GCA} + \text{H}_2\text{O}_2 + \text{UV}$ system.

after six cycles. This result can be attributed primarily to occupation of the active adsorption sites by degradation intermediates [53]. Still, the discoloration in the sixth cycle remained comparable with that in the first cycle. The iron leaching basically remained constant in the range of $0.2\text{--}0.3 \text{ mg L}^{-1}$ in each cycle. The catalyst can be repeatedly used after in-situ regeneration without any special treatment. This also illustrates its good mechanical stability. The geometric confinement structure and the interfacial electronic interaction between $\alpha\text{-FeOOH}$ and GO-CNTs are the primary causes.

Dissolved iron content strongly influences the contaminant degradation kinetics in homogeneous Fenton reactions. The total concentration of dissolved iron species reached 0.213 mg L^{-1} after 5 min irradiation; then it slowly increased to 0.286 mg L^{-1} after 60 min. The relatively low amount of iron leaching from the surface of $\alpha\text{-FeOOH@GCA}$ was recycled directly on the catalyst surface without remarkable diffusion into the solution [39]. Du and coauthors have reported that dissolved iron concentrations were in the range of $0.168\text{--}0.834 \text{ mg L}^{-1}$ when iron oxides were used in the range from 190 to 530 mg L^{-1} for the photoinduced degradation of OII [41]. Fig. 9b shows the discoloration of OII with the maximum leached iron concentration of 0.286 mg L^{-1} . The discoloration rate of OII is clearly slower in the homogeneous photo Fenton system than in the heterogeneous system. It should be noted that the discoloration curve in the homogeneous solution is similar in shape to that of the $\text{UV} + \text{H}_2\text{O}_2$ process (shown in Fig. 4b). The dissolved iron probably contributed little to the discoloration because the leached iron ions quickly hydrolyzed to become less soluble iron (oxy)hydroxides [39,53]. This suggests that the contribution of any homogeneous photo Fenton reaction to discoloration of OII is comparatively insignificant. The adsorption of OII on the surface of $\alpha\text{-FeOOH@GCA}$ plays a dominating role in this surface catalytic process, i.e. the discoloration of OII mainly occurred on the surface of the catalyst.

3.6. Photo-Fenton-like degradation mechanism

3.6.1. Reactive oxygen species involved

The generation of $\bullet\text{OH}$, $\text{O}_2^{\bullet-}$ radicals and $^1\text{O}_2$ in Fenton system has been already confirmed not only through quenching experiments using MeOH, AA and NaN_3 as radical scavengers, respectively [27,54,55], but also proved through spin-trapping electron paramagnetic resonance spectra results [42]. In this study, the quenching effect on discoloration of OII is shown in Fig. 10a. The results show that the discoloration of OII was significantly suppressed in the presence of MeOH, AA or NaN_3 , which suggests that $\bullet\text{OH}$, $\text{O}_2^{\bullet-}$ and $^1\text{O}_2$ are involved in this system. The quenching effect of MeOH implies that activation of H_2O_2 by $\alpha\text{-FeOOH@GCA} + \text{UV}$ can act as a source of $\bullet\text{OH}$ radicals. It shows that $\text{O}_2^{\bullet-}$ is a critical intermediate to $\bullet\text{OH}$ formation and consistent with the observation that the conversion of $\text{O}_2^{\bullet-}$ to $\bullet\text{OH}$ by superoxide-driven Fenton system [27]. The quenching effect of AA suggests that the oxidation of OII by $\text{O}_2^{\bullet-}$ also involved one electron transfer mechanism. That is, photo-generated electrons can quickly transfer on the graphene sheets and captured by adsorbed molecular oxygen to form $\text{O}_2^{\bullet-}$. The subsequent radical reactions can be triggered by the $\text{O}_2^{\bullet-}$. Surface Fe^{2+} oxidation on the catalyst can also be accompanied by further transformation of $\text{O}_2^{\bullet-}$ to $\bullet\text{OH}$, resulting in the oxidation of OII [56]. The quenching effect of NaN_3 can't be neglected indicating $^1\text{O}_2$ also acting as a major ROS in this Fenton system. The generation of $^1\text{O}_2$ may come from the oxidation of $\text{O}_2^{\bullet-}$ or the energy transfer to dissolved O_2 [57]. Quenching effects prove the occurrence of $\bullet\text{OH}$, $\text{O}_2^{\bullet-}$ and $^1\text{O}_2$ radicals; however only quantitative detection of $\bullet\text{OH}$ and $\text{O}_2^{\bullet-}$ was performed and the results are shown in Fig. 10b. The maximum formation concentration of $\bullet\text{OH}$ reached 0.84 mM after 60 min using coumarin as a molecular probe of $\bullet\text{OH}$. The fast formation rate of $\bullet\text{OH}$ (zero-order kinetic rate constant of 0.0136 with $R^2 = 0.998$) reflects the high catalytic activity of $\alpha\text{-FeOOH@GCA}$.

The maximum formation concentration of $O_2^{\bullet-}$ assayed using the radical scavenger TNM was about 0.63 mM at 5 min, after which it remained almost unchanged. The temporal evolutions of $O_2^{\bullet-}$ and $\bullet OH$ were consistent with corresponding quenching results in Fig. 10a. The results show that $\bullet OH$, $O_2^{\bullet-}$ and 1O_2 were the main ROS responsible for the oxidation of OII, which were also proved by spin-trapping electron paramagnetic resonance spectra results in other reports [39,58].

3.6.2. Degradation pathway of OII

To study the changes in molecular structure during OII discoloration, the temporal evolution of the UV–vis spectra was monitored, with the results shown in Fig. 11. The main UV–vis absorption peak was at 485 nm, with a shoulder peak at 430 nm ascribed to n-p* transitions in chromophores containing azo bonds. The shoulders at 254 and 312 nm in the UV region of the peak at 230 nm were assigned to benzene and naphthalene rings, respectively [59]. After 60 min of oxidation there was no significant absorbance in the visible region, presumably owing to the complete destruction of the azo chromophore groups. By contrast, the absorbance peaks at 230 and 312 nm declined gradually, indicating

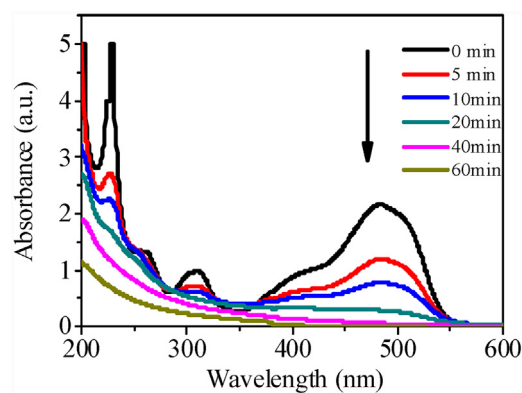


Fig. 11. The evolution of the UV–vis spectra during the degradation of OII in the α -FeOOH@GCA + UV + H_2O_2 system.

that the naphthalene and benzene rings were degraded completely to smaller aliphatic compounds [60]. The TOC left in solution was attributed to intermediates corresponding to the absorption peak near 230 nm in the UV–vis spectrum. There is also no emergence of

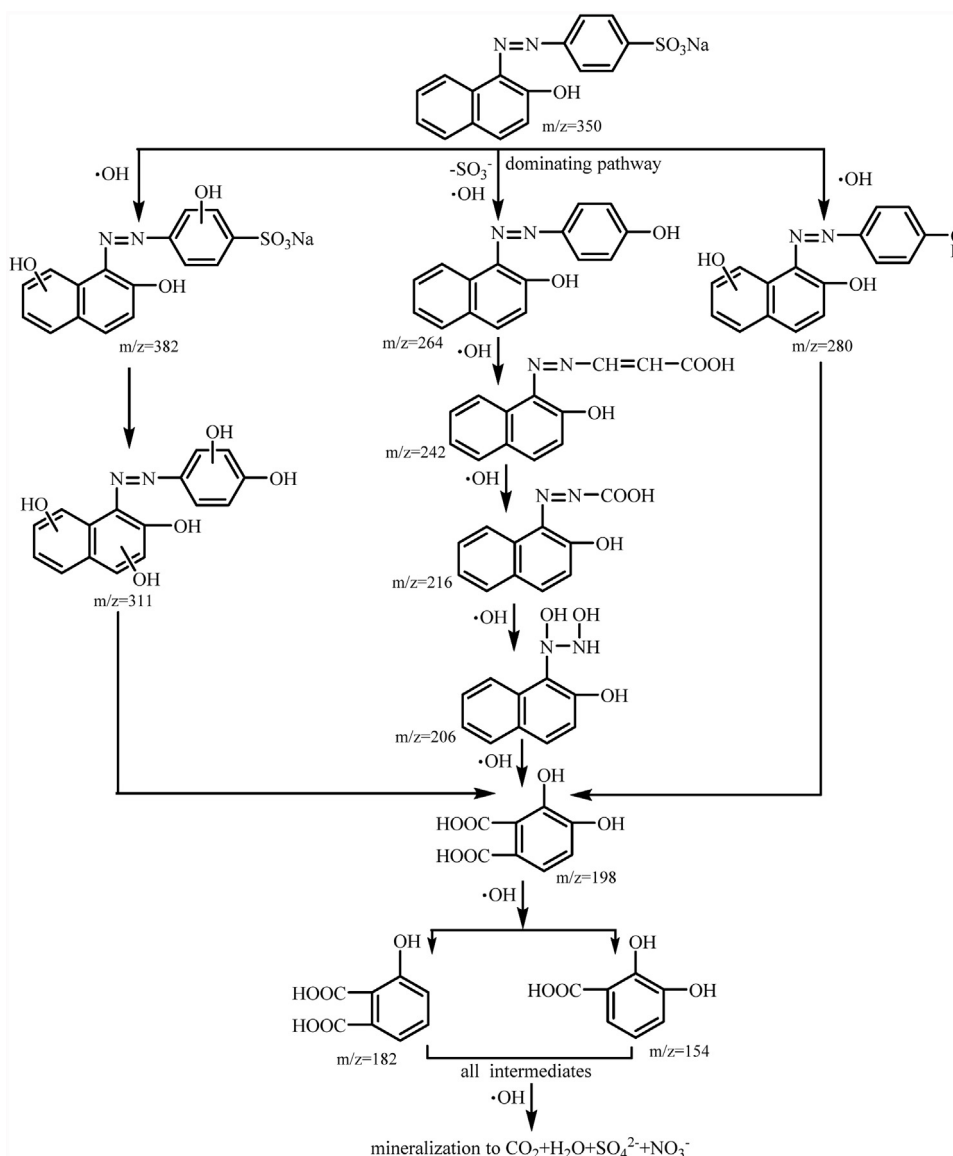


Fig. 12. Proposed degradation pathway of OII in the α -FeOOH@GCA + H_2O_2 + UV system.

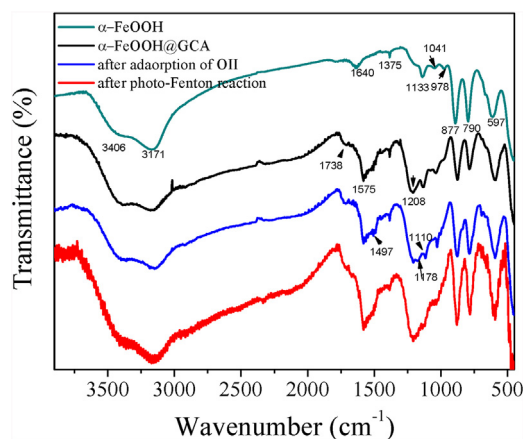


Fig. 13. FTIR spectra of α -FeOOH (green curve), α -FeOOH@GCA before (black curve) or after (blue curve) adsorption of OII and α -FeOOH@GCA after photo-Fenton reaction (red curve) in discoloration of OII. (For interpretation of the references to colour in this figure legend, the reader is referred to the web version of this article.)

any new absorption band or maximum peak shift, proving that the α -FeOOH@GCA + UV + H₂O₂ Fenton process can rapidly and effectively degrade OII. Yao and his coauthors have reported that OII discoloration in a photo Fenton system catalyzed by CuFe₂O₄@C₃N₄ was accompanied by an obvious red shift of the maximum adsorption peak from 485 to 523 nm due to successive demethylation. This may indicate that the degradation pathways and degradation products with CuFe₂O₄@C₃N₄ are different from those with α -FeOOH@GCA [61].

Some reports have identified the degradation intermediates and mineralization products of OII as nitrogen or sulfo-containing compounds, carboxylic acids and anions (sulfate, nitrate and ammonium) [44]. In this study UPLC/MS was used to explore the reaction pathway of OII and identify the degradation intermediates (see Fig. S2). The results suggest the pathway shown in Fig. 12. The degradation begins with cleavage of sulfonate groups by hydroxylation of OII with $m/z=350$ as the dominant reaction pathway, resulting in the formation of fragments corresponding to $m/z=264$, 280 and 311 along with obvious discoloration. The aforementioned dominant degradation pathway and 3 desulfonation intermediates were not reported previously. The large amount of SO₄²⁻ anions generated in the initial 5 min (shown in Fig. 6a) provides additional evidence for the quick elimination of sulfonate groups at initial reaction stage [62]. The aromatic ring structure connected with the sulfonate groups is thereby weakened, and further oxidation leads to ring cleavage yielding species with $m/z=242$. Afterward, the successive oxidation of -N=N- azo bonds yields other organic intermediates and the final mineralization products—nitrate anions. Another secondary probable reaction pathway is the hydroxylation of OII without the rupture of sulfonate groups. The product with $m/z=382$ suggests the generation of hydroxylated OII, which has been earlier reported in literature [62]. Polyhydroxylated intermediates would not be stable. As the reaction proceeds, all such organics will undergo successive oxidation to form smaller short-chain carboxylic acids (acetate, oxalate and formate, etc.), and will finally be mineralized into inorganic species of SO₄²⁻, NO₃⁻, CO₂ and H₂O shown in Fig. 12 [63,64].

3.6.3. FT-IR and XPS evidence

The functional groups on catalyst surface were identified through FTIR. The spectrum of pristine α -FeOOH in Fig. 13 shows that absorbance peaks at 3171 cm⁻¹ and 3406 cm⁻¹ are due to the stretching mode of the hydroxyl portion of the physically adsorbed water or in the envelope of hydrogen-bonded surface OH groups. The peak at 1640 cm⁻¹ is ascribed to bending vibration of H₂O

or OH, implying that entrapped water or OH exists in the bulk α -FeOOH [65,66]. Some peaks in the 900–1200 cm⁻¹ range indicate an iron oxide structure containing one oxygen atom of the sulfate anion to form inner-sphere complexation of sulfate. The XPS of S 2p peaks in Fig. 14 also proved the presence of sulfate in the catalyst. The active ν_1 SO₄ mode band at 978 cm⁻¹ relates to a monodentate complex; the split asymmetric stretch ν_3 SO₄ mode bands at 1133 and at 1041 with a shoulder at 1185 cm⁻¹ relate to a bidentate complex [67–69]. Two characteristic bands recorded at 877 and 790 cm⁻¹ can be indexed to Fe–O–H bending vibrations in the α -FeOOH. The typical IR bands at 597 cm⁻¹ can be indexed to Fe–O stretching vibrations depending on the shape of the α -FeOOH particles [70,71]. Comparing with the IR spectrum of α -FeOOH, the new absorbance peaks of α -FeOOH@GCA indicate C–O stretching vibration in the 1750–1200 cm⁻¹ range. The carbonyl has absorbance bands at 1575 and 1208 cm⁻¹, characteristic of the stretching vibrations bands C=C and the C–O–C in the epoxy. The absorbance of C–O–C and C–O groups of α -FeOOH@GCA apparently indicate strong interfacial interaction of α -FeOOH with oxygen-containing groups of the graphene sheets. After adsorption of OII, the new bands at 1497 and 1178 cm⁻¹ can be attributed to N–N and S–O stretching vibrations of the adsorbed OII, respectively. The band at 1133 cm⁻¹ shifts slightly to 1110 cm⁻¹ due to the exchange interaction of S–O in OII with SO₄ complexed with the α -FeOOH@GCA. After interacting with OII, the peak at 790 cm⁻¹ strengthens. After the OII's photo Fenton degradation, bands at 1497, 1178 and 1110 cm⁻¹ disappear and other bands are basically identical with those of α -FeOOH@GCA [72]. This in-situ regeneration shows that most of adsorbed intermediates or reactants are fully oxidized and desorbed from the surface of catalyst.

The surface element changes and interfacial electronic interactions were investigated using XPS. In Fig. 14, C, Fe, S, N and O are clearly observed in the XPS spectra before and after photocatalytic degradation. Fig. 14 shows the Fe 2p, S 2p and O 1s core-level XPS spectra of α -FeOOH@GCA. The surface iron species were revealed to be Fe 2p_{3/2} and Fe 2p_{1/2} with two satellite peaks evidence of the presence of Fe (III). The constant ratio of doublet Fe 2p shows that the excellent redox recycling of iron oxidation states on the surface of catalyst involves the activation of H₂O₂ [73]. It shows that the synergistic effect of the α -FeOOH@GCA + H₂O₂ + UV system greatly promoted the efficiency of rate-determining step of equation (2). The S 2p binding energy of 168.5 eV agrees well with that of sulfate, proving the presence in α -FeOOH@GCA consistent with the FTIR results [74]. The surface O 1s signal can be deconvoluted into three main peaks at 530.4, 531.7 and 533.0 eV, corresponding to the lattice oxygen Fe–O₂⁻, Fe–O–C linkage, and C–O, respectively, and also indicating the strong interfacial interactions between graphene and α -FeOOH to form strong heterojunction structure [75]. α -FeOOH@GCA would interact with OII on the catalyst's surface through π - π stacking or hydrogen bonds with surface hydroxyl groups to facilitate the photocatalytic process. After photo degradation of the OII there was no noticeable change in the XPS spectra of Fe, O or C. Only the binding energy of nitrogen changed to 400.3 eV, attributable to N-containing degradation intermediates adsorbed on the surface. This too is consistent with the FTIR results and the catalyst reuse experiments. It shows that the stability of α -FeOOH@GCA is essentially unchanged during the photo Fenton reaction.

The heterogeneous Fenton reaction mainly involves Fe²⁺-mediated catalytic H₂O₂ reaction on the surface of iron oxides. Accordingly, a possible Fenton oxidation mechanism for OII discoloration in the α -FeOOH@GCA + H₂O₂ + UV system can be proposed. 1) The OII molecules are adsorbed onto the surface of α -FeOOH@GCA through electrostatic interaction with α -FeOOH or hydrogen bonding and π - π stacking with GO-CNTs. 2) OII oxidation is initiated by •OH produced on the surface of α -FeOOH@GCA [9]. 3)

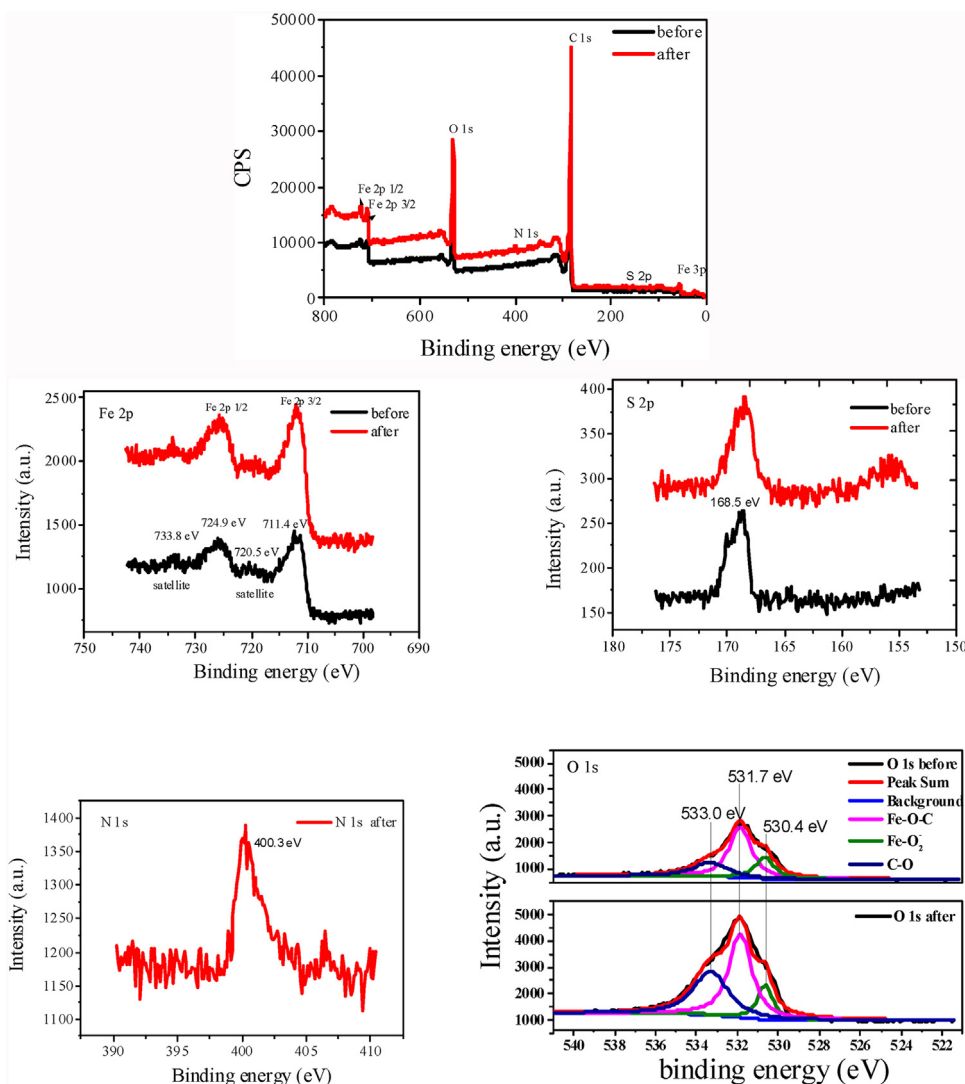


Fig. 14. XPS survey spectra of α -FeOOH@GCA before and after phot-Fenton reaction in discoloration of OII and core-level spectra of Fe 2p, S 2p, N and O 1s before and after photo degradation of OII.

The intermediates then desorb from the surface of the catalyst. The effective cycling of $\text{Fe}^{3+}/\text{Fe}^{2+}$ will facilitate this photo-Fenton-like oxidation efficiency. The cycle between $\text{Fe}^{3+}/\text{Fe}^{2+}$ on the surface of α -FeOOH@GCA is initiated by activation of H_2O_2 by Fe^{2+} to produce $\cdot\text{OH}$ and Fe^{3+} . The Fenton-like catalytic reaction is propagated through photo-reduction of Fe^{3+} to Fe^{2+} accompanying with generating many kinds of radicals besides $\text{O}_2^{\cdot-}$ radicals. The enhanced OII discoloration efficiency was mainly ascribed to the incorporation of GO-CNTs in α -FeOOH@GCA composites. GO-CNTs play important roles in the promotion of photocatalytic activity of α -FeOOH, the presence of GO-CNTs can 1) regulate the crystal growth to control the particle size of α -FeOOH in α -FeOOH@GCA; 2) enhance the light absorption intensity; 3) accelerate the reduction of Fe^{3+} to Fe^{2+} in controlling step of Fenton-like reaction due to presence of presence of interfacial junction in α -FeOOH@GCA [76]. The α -FeOOH@GCA + H_2O_2 + UV system presents a typical photo-assisted surface catalytic heterogeneous Fenton-like reaction.

3.7. Toxicity and environmental applications

In general, the oxidation of organic contaminants changes their toxicity for living organisms [77,78]. Here, the luminous bacterium *Vibrio qinghaiensis* was used to assess the samples' toxicity. In Fig.

S3, the relative luminosity increased continuously from 30.1% to 57% after 60 min, suggesting that the toxicity of the intermediates decreased with time. Luna and his colleagues have reported [79] that the toxicity of the products from OII oxidation continues to decrease, similar to the results observed in the discoloration of OII over Al-pillared Fe-smectite in a heterogeneous photo-Fenton system [80]. The decreasing toxicity may relate to the formation of less toxic degradation products [81,82].

The presence of the GO-CNTs carrier expands the light absorption by α -FeOOH within the visible range. The visible-light-driven discoloration of OII by α -FeOOH@GCA and H_2O_2 were compared using irradiation with a 100 W iodine-tungsten lamp with wavelength >400 nm. As shown in Fig. S4a, the pseudo-first order kinetic constant was 0.042 min^{-1} ($R^2 = 0.950$) in the presence of the α -FeOOH@GCA compared with almost no discoloration with H_2O_2 . The quantum yield of α -FeOOH@GCA + H_2O_2 + Visible light system was about 0.33%. The extent of OII discoloration (expressed as % degradation) was almost the same in α -FeOOH@GCA + H_2O_2 + Visible light driven system whether using UV filter with wavelength more than 420 nm (shown in Fig. 4Sb) or not. The lower discoloration rate of OII was probably related with the lower $\cdot\text{OH}$ quantum yield under longer irradiation wavelength. The light-induced oxidation of OII mainly occurs through

ligand metal complexing transition [83]. α -FeOOH@GCA shows super-fast visible-driven catalytic activity based on its outstanding photosensitivity in the visible region compared with similar materials reported in previous studies, such as Fly ash-Fe³⁺ [84], Bentonite-Fe [85], activated carbon aerogel-Fe [86], ZnFe₂O₄-rGO [87], Cu₂O-rGO [41], Fe₃O₄-rGO [88], Fe₂O₃-rGO [75], and β -FeOOH-rGO [89]. This recommends α -FeOOH@GCA for further consideration for practical solar remediation applications, as about 40% of the solar spectrum is in the visible range.

4. Conclusions

A novel aerogel matrix catalyst of α -FeOOH@GCA incorporating GO-CNTs and α -FeOOH nanoparticles was successfully synthesized through an in-situ Fe²⁺-reduction induced self-assembly process. The activation of H₂O₂ by α -FeOOH@GCA and UV₃₆₅ was proved to be more efficient. Comparing with α -FeOOH nanoparticles, the greatly enhanced catalytic activity in OII discoloration in α -FeOOH@GCA + H₂O₂ + UV₃₆₅ system was ascribed to the well chemically coupled composite structure of α -FeOOH and GO-CNTs. α -FeOOH@GCA can overcome the intrinsic disadvantage of homogeneous Fenton reaction, be feasible and effective in destroying various structurally different organic pollutants, such as MB, RdB, OII, phenol and BPA, and has excellent durability throughout 6 consecutive reuse cycles under this typical photo-Fenton operating conditions. The elimination of the luminescent bacteria acute toxicity during the treatment was correlated with the evolution and disappearance of less toxic degradation intermediates of OII, which shows that this photo-Fenton process would not produce secondary pollutants when the process is used under optimized conditions. It should be a viable technology for degrading and detoxifying high concentrations of dyes and their by-products in textile wastewater without end-of-pipe discharge of the iron sludge into the environment. The application and improvement of α -FeOOH@GCA in visible light-driven processes of OII discoloration would be highly expected in future for utilizing solar energy. α -FeOOH@GCA can be a good candidate to effectively enhance the photocatalytic activity of pristine α -FeOOH through the formation of synergistically functioning composite with graphene oxide nanosheets and carbon nanotubes. This study provides an alternative technology to improve the catalytic efficiency and environmental application of natural metal oxides through synthesis of advanced composites with graphene-based materials.

Acknowledgement

This research was financed by the National Natural Science Foundation of China (grant 21377039).

Appendix A. Supplementary data

Supplementary data associated with this article can be found, in the online version, at <http://dx.doi.org/10.1016/j.apcatb.2017.05.019>.

References

- [1] S. Chowdhury, R. Balasubramanian, Appl. Catal. B—Environ. 160 (2014) 307–324.
- [2] P. Mazellier, M. Bolte, J. Photochem. Photobiol. A—Chem. 132 (2000) 129–135.
- [3] J.Y. Feng, X.J. Hu, P.L. Yue, Environ. Sci. Technol. 38 (2004) 5773–5778.
- [4] S.R. Pouran, A.A.A. Raman, W. Daud, J. Clean Prod. 64 (2014) 24–35.
- [5] H.B. Hadjiltaief, P. Da Costa, M.E. Galvez, M. Ben Zina, Ind. Eng. Chem. Res. 52 (2013) 16656–16665.
- [6] J.Y. Feng, X.J. Hu, P.L. Yue, H.Y. Zhu, G.Q. Lu, Ind. Eng. Chem. Res. 42 (2003) 2058–2066.
- [7] J.H. Ramirez, C.A. Costa, L.M. Madeira, G. Mata, M.A. Vicente, M.L. Rojas-Cervantes, A.J. Lopez-Peinado, R.M. Martin-Aranda, Appl. Catal. B—Environ. 71 (2007) 44–56.
- [8] J. Herney-Ramirez, M.A. Vicente, L.M. Madeira, Appl. Catal. B—Environ. 98 (2010) 10–26.
- [9] J. Feng, X.J. Hu, P.L. Yue, Environ. Sci. Technol. 38 (2004) 269–275.
- [10] R. Leary, A. Westwood, Carbon 49 (2011) 741–772.
- [11] S. Iijima, Nature 354 (1991) 56–58.
- [12] Y. Chen, B. Zhang, G. Liu, X.D. Zhuang, E.T. Kang, Chem. Soc. Rev. 41 (2012) 4688–4707.
- [13] L. Xiao, D.Q. Wu, S. Han, Y.S. Huang, S. Li, M.Z. He, F. Zhang, X.L. Feng, ACS Appl. Mater. Interfaces 5 (2013) 3764–3769.
- [14] W.J. Han, L. Ren, L.J. Gong, X. Qi, Y.D. Liu, L.W. Yang, X.L. Wei, J.X. Zhong, ACS Sustain. Chem. Eng. 2 (2014) 741–748.
- [15] Z.Y. Sui, Q.H. Meng, X.T. Zhang, R. Ma, B. Cao, J. Mater. Chem. 22 (2012) 8767–8771.
- [16] D.T. Pham, T.H. Lee, D.H. Luong, F. Yao, A. Ghosh, V.T. Le, T.H. Kim, B. Li, J. Chang, Y.H. Lee, ACS Nano 9 (2015) 2018–2027.
- [17] S.B. Ye, J.C. Feng, ACS Appl. Mater. Interfaces 6 (2014) 9671–9679.
- [18] J. Li, F. Wang, C.Y. Liu, J. Colloid Interface Sci. 382 (2012) 13–16.
- [19] M.A. Worsley, P.J. Pauzaskie, T.Y. Olson, J. Biener, J.H. Satcher, T.F. Baumann, J. Am. Chem. Soc. 132 (2010) 14067–14069.
- [20] X.T. Zhang, Z.Y. Sui, B. Xu, S.F. Yue, Y.J. Luo, W.C. Zhan, B. Liu, J. Mater. Chem. 21 (2011) 6494–6497.
- [21] W.F. Chen, L.F. Yan, Nanoscale 3 (2011) 3132–3137.
- [22] H.P. Cong, X.C. Ren, P. Wang, S.H. Yu, ACS Nano 6 (2012) 2693–2703.
- [23] Y.X. Xu, K.X. Sheng, C. Li, G.Q. Shi, ACS Nano 4 (2010) 4324–4330.
- [24] C.H. Kim, B.H. Kim, K.S. Yang, Carbon 50 (2012) 2472–2481.
- [25] W.S. Hummers, R.E. Offeman, J. Am. Chem. Soc. 80 (1958) 1339.
- [26] R.M. Sellers, Analyst 105 (1980) 950–954.
- [27] D.H. Kim, A.D. Bokare, M.S. Koo, W. Choi, Environ. Sci. Technol. 49 (2015) 3506–3513.
- [28] H. Czili, A. Horvath, Appl. Catal. B—Environ. 81 (2008) 295–302.
- [29] J. Rabani, W.A. Mulac, M.S. Matheson, J. Phys. Chem. 69 (1965) 53–70.
- [30] H.T. Tian, J.W. Li, M. Ge, Y.P. Zhao, L. Liu, Catal. Sci. Technol. 2 (2012) 2351–2355.
- [31] T.A. Vu, M.M. Reagan, D.S. Li, B. Legg, J.J. De Yoreo, J.F. Banfield, H.Z. Zhang, CrystEngComm 16 (2014) 1466–1471.
- [32] J. Dousma, D.D. Ottelander, P.L.D. Bruyn, J. Inorg. Nucl. Chem. 41 (1979) 1565–1568.
- [33] Q.F. Zheng, Z.Y. Cai, Z.Q. Ma, S.Q. Gong, ACS Appl. Mater. Interfaces 7 (2015) 3263–3271.
- [34] H. Wang, S. Li, Y.M. Si, Z.Z. Sun, S.Y. Li, Y.H. Lin, J. Mat. Chem. B 2 (2014) 4442–4448.
- [35] Z. Fan, D.Z.Y. Tng, C.X.T. Lim, P. Liu, S.T. Nguyen, P.F. Xiao, A. Marconnet, C.Y.H. Lim, H.M. Duong, Colloid Surf. A—Physicochem. Eng. Asp. 445 (2014) 48–53.
- [36] F. Duarte, F.J. Maldonado-Hodar, A.F. Perez-Cadenas, L.M. Madeira, Appl. Catal. B—Environ. 85 (2009) 139–147.
- [37] B. Tryba, A.W. Morawski, M. Inagaki, M. Toyoda, Appl. Catal. B—Environ. 63 (2006) 215–221.
- [38] W.P. Du, Y.M. Xu, Y.S. Wang, Langmuir 24 (2008) 175–181.
- [39] J. He, W.H. Ma, J.J. He, J.C. Zhao, J.C. Yu, Appl. Catal. B—Environ. 39 (2002) 211–220.
- [40] H.C. Lan, A.M. Wang, R.P. Liu, H.J. Liu, J.H. Qu, J. Hazard. Mater. 285 (2015) 167–172.
- [41] W.X. Zou, L. Zhang, L.C. Liu, X.B. Wang, J.F. Sun, S.G. Wu, Y. Deng, C.J. Tang, F. Gao, L. Dong, Appl. Catal. B—Environ. 181 (2016) 495–503.
- [42] Y.Y. Gao, X.P. Pu, D.F. Zhang, G.Q. Ding, X. Shao, J. Ma, Carbon 50 (2012) 4093–4101.
- [43] H.G. Fan, X.T. Zhao, J.H. Yang, X.N. Shan, L.L. Yang, Y.J. Zhang, X.Y. Li, M. Gao, Catal. Commun. 29 (2012) 29–34.
- [44] N. Inchaurredo, J. Font, C.P. Ramos, P. Haure, Appl. Catal. B—Environ. 181 (2016) 481–494.
- [45] J. Fernandez, J. Bandara, A. Lopez, P. Buffat, J. Kiwi, Langmuir 15 (1999) 185–192.
- [46] G.V. Buxton, C.L. Greenstock, W.P. Helman, A.B. Ross, J. Phys. Chem. Ref. Data 17 (1988) 513–886.
- [47] M.W. Laipan, R.L. Zhu, J.X. Zhu, H.P. He, J. Mol. Catal. A—Chem. 415 (2016) 9–16.
- [48] W. Baran, A. Makowski, W. Wardas, Dyes Pigments 76 (2008) 226–230.
- [49] A.R. Khataee, M.B. Kasiri, J. Mol. Catal. A—Chem. 328 (2010) 8–26.
- [50] O. Kerkez-Kuyumcu, E. Kibar, K. Dayioglu, F. Gedik, A.N. Akin, S. Ozkara-Aydinoglu, J. Photochem. Photobiol. A—Chem. 311 (2015) 176–185.
- [51] M.A. Rauf, S.S. Ashraf, Chem. Eng. J. 151 (2009) 10–18.
- [52] Y. Shen, Q.L. Fang, B.L. Chen, Environ. Sci. Technol. 49 (2015) 67–84.
- [53] Y. Li, F.S. Zhang, Chem. Eng. J. 158 (2010) 148–153.
- [54] L.L. Bissey, J.L. Smith, R.J. Watts, Water Res. 40 (2006) 2477–2484.
- [55] B.A. Smith, A.L. Teel, R.J. Watts, Environ. Sci. Technol. 38 (2004) 5465–5469.
- [56] D.W. King, H.A. Lounsbury, F.J. Millero, Environ. Sci. Technol. 29 (1995) 818–824.
- [57] Q. Liu, Y. Guo, Z. Chen, Z. Zhang, X. Fang, Appl. Catal. B: Environ. 183 (2016) 231–241.
- [58] S.K. Han, T.M. Hwang, Y. Yoon, J.W. Kang, Chemosphere 84 (2011) 1095–1101.
- [59] Y.I. Hou, J.H. Qu, X. Zhao, P.J. Lei, D.J. Wan, C.P. Huang, Sci. Total Environ. 407 (2009) 2431–2439.
- [60] J.Y. Feng, X.J. Hu, P.L. Yue, H.Y. Zhu, G.Q. Lu, Water Res. 37 (2003) 3776–3784.

- [61] Y.J. Yao, F. Lu, Y.P. Zhu, F.Y. Wei, X.T. Liu, C. Lian, S.B. Wang, *J. Hazard. Mater.* 297 (2015) 224–233.
- [62] P. Bansal, D. Singh, D. Sud, *Sep. Purif. Technol.* 72 (2010) 357–365.
- [63] M. Karkmaz, E. Puzenat, C. Guillard, J.M. Herrmann, *Appl. Catal. B—Environ.* 51 (2004) 183–194.
- [64] S. Bilgi, C. Demir, *Dyes Pigments* 66 (2005) 69–76.
- [65] J.-F. Boily, J. Szanyi, A.R. Felmy, *Geochim. Cosmochim. Acta* 70 (2006) 3613–3624.
- [66] J.-F. Boily, A.R. Felmy, *Geochim. Cosmochim. Acta* 72 (2008) 3338–3357.
- [67] C. Morterra, A. Chiorlino, E. Borello, *Mater. Chem. Phys.* 10 (1984) 119–138.
- [68] G.Y. Zhang, D. Peak, *Geochim. Cosmochim. Acta* 71 (2007) 2158–2169.
- [69] S.J. Hug, *J. Colloid Interface Sci.* 188 (1997) 415–422.
- [70] M. Ristic, S. Music, M. Godec, *J. Alloy Compd.* 417 (2006) 292–299.
- [71] S. Kabiri, D.N.H. Tran, T. Altalhi, D. Losic, *Carbon* 80 (2014) 523–533.
- [72] L. Lucarelli, V. Nadtochenko, J. Kiwi, *Langmuir* 16 (2000) 1102–1108.
- [73] X.M. Zhou, H.C. Yang, C.X. Wang, X.B. Mao, Y.S. Wang, Y.L. Yang, G. Liu, *J. Phys. Chem. C* 114 (2010) 17051–17061.
- [74] L.T. Weng, P. Bertrand, J.H. Stone-Masui, W.E.E. Stone, *Langmuir* 13 (1997) 2943–2952.
- [75] P.H. Shao, J.Y. Tian, B.R. Liu, W.X. Shi, S.S. Gao, Y.L. Song, M. Ling, F.Y. Cui, *Nanoscale* 7 (2015) 14254–14263.
- [76] M. Vinothkannan, C. Karthikeyan, G.G. Kumar, A.R. Kim, D.J. Yoo, *Spectrochim. Acta Part. A—Mol. Biomol. Spectrosc.* 136 (2015) 256–264.
- [77] H.R. Buser, T. Poiger, M.D. Muller, *Environ. Sci. Technol.* 33 (1999) 2529–2535.
- [78] P.K. Wong, P.Y. Yuen, *Water Res.* 30 (1996) 1736–1744.
- [79] L.A.V. de Luna, T.H.G. da Silva, R.F.P. Nogueira, F. Kummrow, G.A. Umbuzeiro, *J. Hazard. Mater.* 276 (2014) 332–338.
- [80] H.Y. Li, Y.L. Li, L.J. Xiang, Q.Q. Huang, J.J. Qiu, H. Zhang, M.V. Sivaiah, F. Baron, J. Barrault, S. Petit, S. Valange, *J. Hazard. Mater.* 287 (2015) 32–41.
- [81] R. Andreozzi, M. Canterino, R. Lo Giudice, R. Marotta, G. Pinto, A. Pollio, *Water Res.* 40 (2006) 630–638.
- [82] H. Chaabane, E. Vullet, F. Joux, F. Lantoine, P. Conan, J.F. Cooper, C.M. Coste, *Water Res.* 41 (2007) 1781–1789.
- [83] B.C. Faust, J. Hoigné, *Atmos. Environ. Part A. Gen. Top.* 24 (1990) 79–89.
- [84] Y. Flores, R. Flores, A. Alvarez Gallegos, *J. Mol. Catal. A—Chem.* 281 (2008) 184–191.
- [85] Y. Gao, Y. Wang, H. Zhang, *Appl. Catal. B: Environ.* 178 (2015) 29–36.
- [86] J.H. Ramirez, F.J. Maldonado-Hodar, A.F. Perez-Cadenas, C. Moreno-Castilla, C.A. Costa, L.M. Madeira, *Appl. Catal. B—Environ.* 75 (2007) 312–323.
- [87] Y. Fu, X. Wang, *Ind. Eng. Chem. Res.* 50 (2011) 7210–7218.
- [88] B. Qiu, Q. Li, B. Shen, M. Xing, J. Zhang, *Appl. Catal. B—Environ.* 183 (2016) 216–223.
- [89] F. Xiao, W. Li, L. Fang, D. Wang, *J. Hazard. Mater.* 308 (2016) 11–20.